

# Controlled Synthesis of Pure-Phase GaAs Nanowires through Shear Tension

Yubin Kang,<sup>#</sup> Guangren Na,<sup>#</sup> Dengkui Wang, Jilong Tang, Lijun Zhang, Yabing Shan, Chunxiao Cong, Zhipeng Wei,<sup>\*</sup> and Rui Chen<sup>\*</sup>



Cite This: *ACS Photonics* 2021, 8, 2889–2897



Read Online

ACCESS |



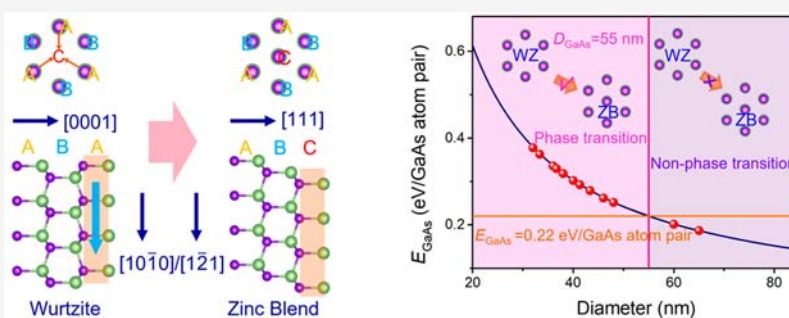
Metrics & More



Article Recommendations



Supporting Information



**ABSTRACT:** The identical crystal phase is one of the most critical and challenging subjects in the fabrication of low dimensional III–V semiconductors for electronic and optoelectronic applications. The polytype boundaries induced by the coexistence of wurtzite (WZ) and zinc blende (ZB) phases in the nanowire (NW) limits the device performance. It is interesting to find that the epitaxially grown GaAsSb shell outside the WZ/ZB mixed-phase GaAs NW will induce the complete transformation of WZ segments of GaAs to ZB structures due to the shear tension. The underlying physical mechanism was proposed and verified by first-principle transition barrier calculations and the Shockley partial dislocations theory. Based on the fabricated pure-phase NW, a proof-of-concept high-performance avalanche photodiode was demonstrated, which shows responsivity and a multiplication factor up to  $3.3 \times 10^3$  A/W and  $8.62 \times 10^3$  at  $-11.5$  V, respectively. This work promises shear tension as an effective strategy for the controlled syntheses of single-phase semiconductor NWs and other nanostructures.

**KEYWORDS:** III–V semiconductor nanowire, shear tension, crystal phase, strain, molecular beam epitaxy

In the past decades, III–V semiconductors have drawn extensive research interest due to their unique properties as well as various applications in electronics,<sup>1</sup> photonics,<sup>2</sup> and life sciences.<sup>3</sup> The development of nanotechnology enables the materials for superior electrical and optical properties, which have been utilized for nanowire (NW) photodetectors,<sup>4,5</sup> transistors,<sup>6</sup> light-emitting diodes,<sup>7</sup> solar cells,<sup>8</sup> lasers,<sup>9</sup> single-electron memory devices,<sup>10</sup> and DNA detectors.<sup>11</sup> It is known that the cubic zinc blende (ZB) phase is the only stable phase in bulk III–V semiconductors. However, with the decrease of dimension, the hexagonal wurtzite (WZ) phase appears. It is reported that a higher ON–OFF ratio has been observed in WZ InAs NW transistors.<sup>12,13</sup> Therefore, the existence of the WZ structure of III–V materials at a low dimension opens the possibility to tune the properties of material through the crystal phase. Unfortunately, ZB and WZ structures always coexist with each other and accompany defects like stacking faults and twins,<sup>14–16</sup> which greatly influence the properties of the materials and devices.<sup>17–19</sup> The WZ/ZB mixed-phase structure greatly decreases the carrier recombination efficiency, carrier lifetime, and carrier mobility of the materials.<sup>17–22</sup> Therefore,

elimination of WZ/ZB mixed-phases and structure defects is of great significance for improving the properties of NWs and device performance.

It is known that the mixed-phases and stacking faults in GaAs NWs are created due to the energy perturbation during the growth process. Therefore, controlling or eliminating the perturbation is an effective way to achieve the perfect single-phase GaAs NWs. Up until now, the fabrication of pure-phase NWs has been realized by precise regulation of parameters during growth, such as growth temperature,<sup>23–25</sup> V/III flux ratio,<sup>26,27</sup> droplet shape,<sup>28–30</sup> annealing temperature,<sup>31,32</sup> epitaxial burying,<sup>33</sup> and doping.<sup>22,34–37</sup> Researchers control the energy perturbation through seeking an appropriate growth

Received: August 5, 2021

Published: October 7, 2021



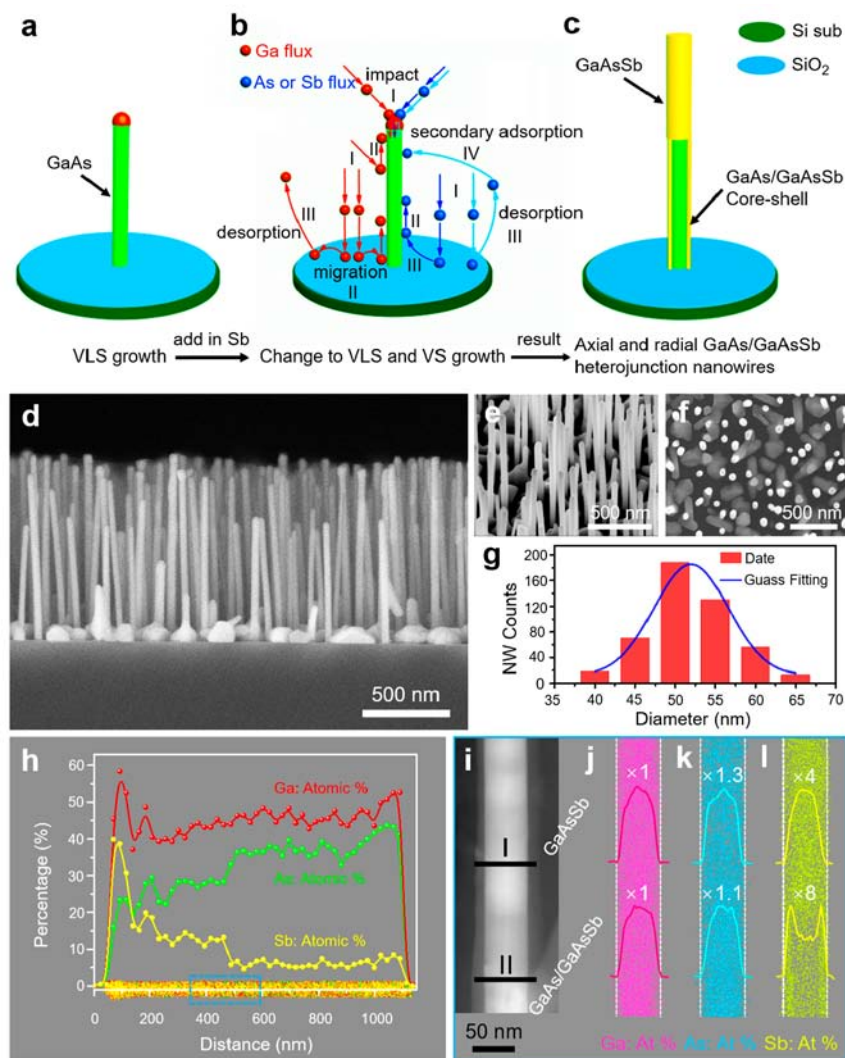


**Figure 1.** Growth mechanism, morphology, and structure of the GaAs/GaAsSb NWs. (a) Self-catalyzed GaAs NWs are grown by the VLS growth mechanism. (b) After adding Sb, the GaAs/GaAsSb NWs are grown by VLS and VS mechanisms. (c) Schematic diagram of the GaAs/GaAsSb NWs. (d–f) The side-view, 45° tilted, and top-view SEM images of GaAs/GaAsSb NWs grown on the Si(111) substrate. (g) The diameter distribution of GaAs/GaAsSb NWs. (h) EDXs mapping and axial line scanning of a single GaAs/GaAsSb NW; Ga (red), As (green), and Sb (yellow). (i) HAADF STEM micrograph of the segment highlighted in the blue frame of (h). EDXs mapping and line scanning of (j) Ga, (k) As, and (l) Sb elements across the black lines in (i). The element percentages are normalized.

window. However, the successful fabrication of the pure-phase structure by the above methods is complicated due to the small growth window and difficult control. Seeking an easier and repeatable method to fabricate pure-phase crystalline samples is urgent.

We herein report an interesting investigation to control the aforementioned energy perturbation during the growth of GaAs NWs through shear tension. The ZB GaAsSb shell is grown on the mixed-phases GaAs core by molecular beam epitaxy (MBE). Due to the strain induced by the atomic arrangement difference between GaAs (WZ) and GaAsSb (ZB), the Ga–As planes slip and promote the rearrangement of atomic planes to achieve pure-phase. The phase transition of GaAs from WZ to ZB has been clearly revealed by Raman spectroscopy and high-resolution transmission electron microscopy (HRTEM) characterizations. Based on the synthesized pure-phase GaAs NWs, a high-performance GaAs/GaAsSb NW avalanche photodiode (APD) has been demonstrated. The APD shows a high responsivity of  $3.3 \times$

$10^3$  A/W and a multiplication factor up to  $8.62 \times 10^3$  under a reverse bias of 11.5 V at room temperature. Our research proposed a new crystal structure regulation method, which is beneficial for nanomaterials preparation and device applications.

## RESULTS AND DISCUSSION

A self-catalyzed vapor–liquid–solid (VLS) growth mechanism and catalyst-free vapor–solid (VS) growth mechanism are applied during the NWs growth. First, vertical GaAs NWs are grown by a VLS mechanism where Ga droplets are served as a catalyst. Then, the Sb source is introduced and the GaAsSb structures are grown. It is needed to mention that the GaAsSb structures follow two different mechanisms during the growth, corresponding to form pure GaAsSb NWs on top of the initial GaAs NWs and the GaAsSb shell layer outside the GaAs NWs. The GaAsSb NWs are grown based on the VLS growth mechanism, and the growth of GaAsSb NWs is terminated under Sb overpressure. Finally, GaAsSb NWs with high Sb

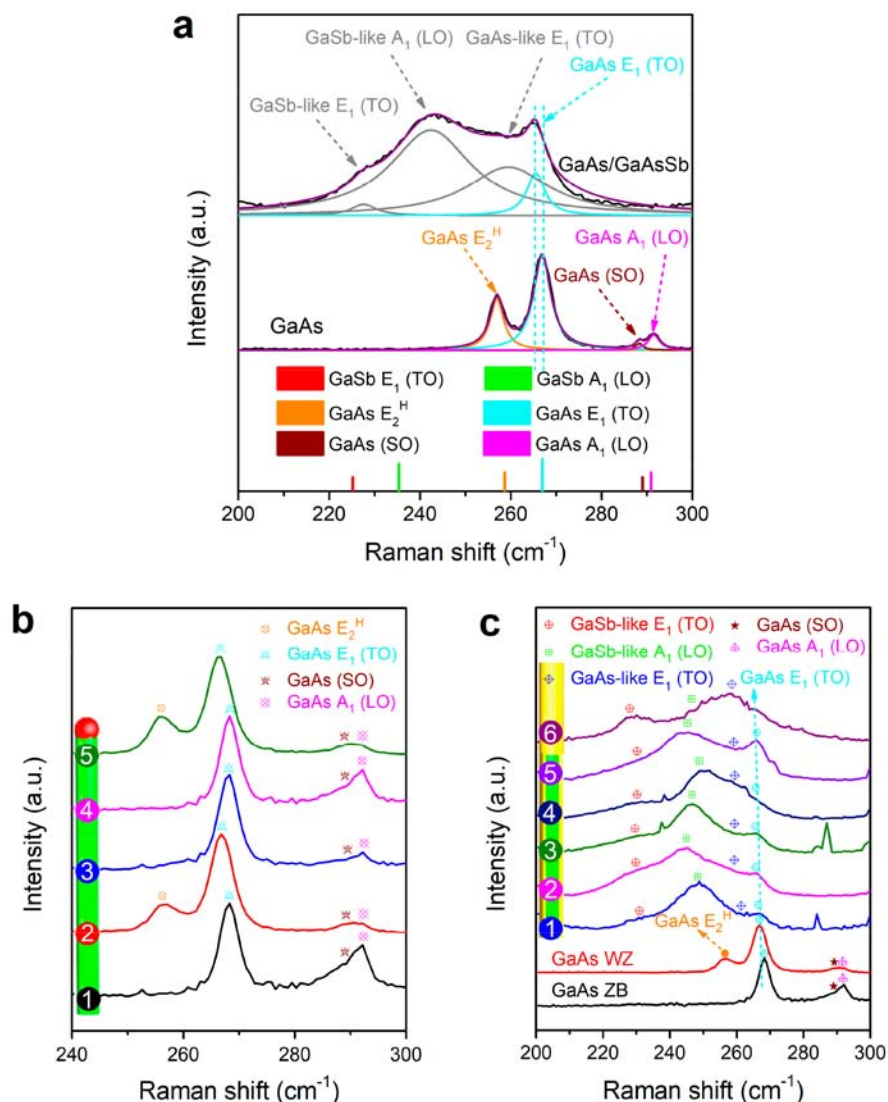


**Figure 2.** Raman spectra of GaAs and GaAs/GaAsSb NW. (a) The Raman spectra of GaAs and GaAs/GaAsSb core-shell NWs. Standard GaAs and GaSb related mode peaks are used as reference. The resolved peaks are fitted by multi-Lorentzian functions.  $\mu$ -Raman spectra of the different locations along (b) a single GaAs NW and (c) a single GaAs/GaAsSb core-shell NW.

composition are formed, while the GaAsSb shells are grown by the VS growth mechanism. The detailed growth mechanism of GaAs/GaAsSb NWs is shown in Figure 1a–c, and the growth conditions can be found in the Supporting Information. The morphology and crystallization properties of the GaAs/GaAsSb NWs are studied by scanning electron microscopy (SEM) and shown in Figure 1d–f. The length of the NWs is about 1.0  $\mu\text{m}$ , while the diameter follows the Gaussian distribution with an average value of 52 nm (Figure 1g). A morphology characterization of the as-grown GaAs NWs without GaAsSb is shown in Figure S1. The average diameter and length of GaAs NWs are around 43 nm and 1.3  $\mu\text{m}$ , respectively.

The energy-dispersive X-ray (EDX) line scanning of a single GaAs/GaAsSb NW is shown in Figure 1h. The whole NW composes of three elements, Ga, As, and Sb, with a high Sb component at the top and a low one at the bottom. The EDX mapping of the whole NW is shown in Figure S2. The high-resolution, high-angle annular dark field (HAADF) scanning transmission electron microscopy (STEM) fragment of a

middle section of a GaAs/GaAsSb NW (as indicated by blue frame in Figure 1h) is shown in Figure 1i. The line scanning collected from two different positions labeled as I and II are plotted in Figure 1j–l. The Ga is homogeneously distributed over the sample (Figure 1j), while the Sb is more concentrated at the shell layer of the bottom segment (Figure 1l). The curves indicate that position I is GaAsSb NW, while position II is the GaAs/GaAsSb core-shell structure. Based on the characterization, the Sb composition of the GaAsSb shell is determined to be around 0.15–0.18 (Figure S3), and the thickness of the GaAsSb shell at position II is around 8 nm.

To understand the structural change of the GaAs NW before and after GaAsSb shell growth, confocal  $\mu$ -Raman spectroscopy is employed. The Raman spectra and multi-Lorentzian fitting of the single GaAs NW and GaAs/GaAsSb NW are shown in Figure 2a. It is known that the WZ GaAs structure can be determined by the characteristic peak of the  $E_2^H$  mode. Figure 2a shows that the Raman scattering of the GaAs NW is composed of  $E_2^H$ ,  $E_1$  (TO), surface optical (SO), and  $A_1$  (LO) mode at 257.1, 267, 288.3, and 291.4  $\text{cm}^{-1}$ , respectively. This

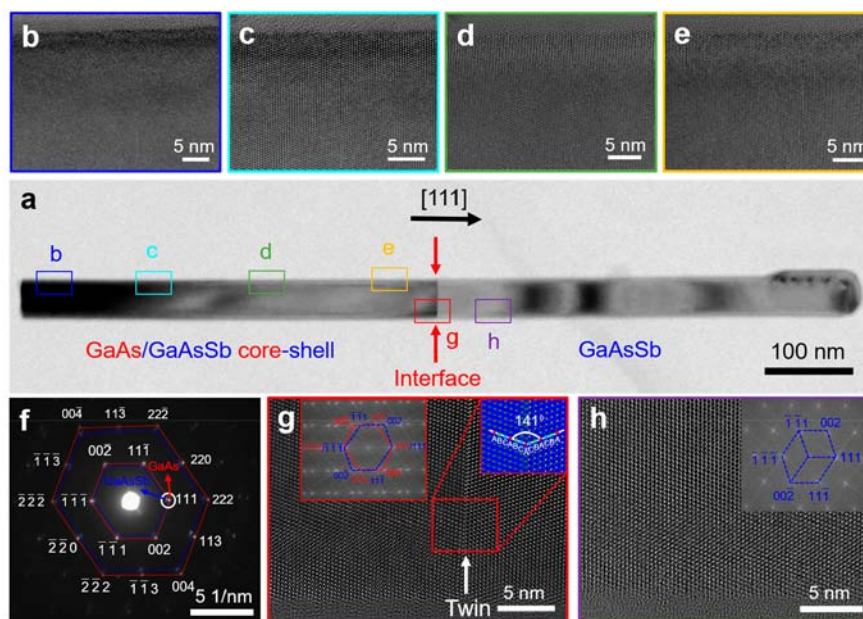


**Figure 3.** Crystal structure of GaAs/GaAsSb NW. (a) TEM image of a typical GaAs/GaAsSb NW with a diameter of  $\sim 50$  nm. (b–h) HRTEM images taken along the  $[111]$  zone axis from the bottom to middle regions of the GaAs/GaAsSb NW in (a). The interface of the heterojunction is indicated by red arrows. (b–e) HRTEM images of the GaAs/GaAsSb core-shell NW. (f) Typical SAED pattern of the selected region of the NW from panel (d). (g) HRTEM image of the GaAs/GaAsSb heterojunction interface. A twin plane is indicated by a white arrow. Inset shows the corresponding temperature colored details and FFT pattern. (h) HRTEM image of GaAsSb NW and the inset showing its FFT pattern.

is consistent with previously reported literature,<sup>14,15,38</sup> as shown in the inset of Figure 2a. In addition, the Raman characterizations of large-area GaAs NWs shown in Figures S4 and S5 can also find the  $E_2^H$  mode, which indicates the presence of WZ structure in the bare GaAs NWs. For the Raman measurement of GaAs/GaAsSb NW, three gray peaks at low frequency are found to be related to GaAsSb, namely, GaSb-like  $E_1$  (TO), GaSb-like  $A_1$  (LO), and GaAs-like  $E_1$  (TO), respectively. The peak located at  $260\text{ cm}^{-1}$  can be ascribed to the GaAs  $E_1$  (TO) mode, while the blue-shift of the peak can be ascribed to the replacement of As with Sb. The peak at  $265.5\text{ cm}^{-1}$  can be assigned to the  $E_1$  (TO) mode of the GaAs core.  $E_1$  (TO) mode of GaAs NW and core is marked with a cyan dashed line. The red-shift of the GaAs  $E_1$  (TO) mode indicates that the GaAs core suffers with tensile stress.<sup>39–41</sup> It is worth noting that the  $E_2^H$  mode of the GaAs core is absent in the GaAs/GaAsSb core-shell structure, which implies the disappearance of the WZ GaAs structure. Similar results have been recorded for the Raman data of large-area GaAs/GaAsSb NWs shown in Figures S6 and S7.

The  $\mu$ -Raman characterizations of various positions on the bare GaAs NW (Figure 2b) are carried out to analyze the structure of GaAs with or without shell. The crystal phase of positions 1, 3, and 4 belong to the ZB structure and the other two are WZ structure, which is distinguished by structural characteristic peak of  $E_2^H$  mode. For an easier comparison, the Raman spectra of WZ and ZB GaAs are plotted. As shown in Figure 2c, a single GaAs/GaAsSb core-shell NW displays the modes of GaSb-like  $E_1$  (TO), GaSb-like  $A_1$  (LO), GaAs-like  $E_1$  (TO), and GaAs  $E_1$  (TO). The red-shift of the GaAs  $E_1$  (TO) mode implies that the whole GaAs core suffers tensile stress. In addition, no  $E_2^H$  mode has been observed in the GaAs/GaAsSb core-shell NW, which indicates that the GaAs core is a pure ZB structure.<sup>42,43</sup> More characterizations of NWs have been

performed, and similar results have been obtained, which can be found in Figures S8 and S9.

To further verify the structure of the NW, TEM characterization was performed on single GaAs/GaAsSb core-shell NW is shown in Figure 3. Figure 3a shows a bright-field TEM image of typical GaAs/GaAsSb NW. The interface of the heterojunction is indicated by red arrows. The left region of the arrow is GaAs/GaAsSb core-shell structure while the right is GaAsSb NW. From the results shown in Figure 3b–e, the core-shell NW possesses same crystal orientation without stacking faults. In addition, the GaAs/GaAsSb core-shell structure and ZB crystal phase are also verified by selected area electron diffraction (SAED) shown in Figure 3f. The diffraction spots and crystal orientations of the GaAs core and GaAsSb shell are marked as red and blue, respectively. The HRTEM of other positions on GaAs/GaAsSb core-shell NW can be found in Figure S10. Therefore, it is concluded that the GaAs/GaAsSb core-shell NW is of a pure ZB structure. Many other GaAs/GaAsSb core-shell NWs are measured (Figures S11–S15), and the large-area Raman characterization of GaAs/GaAsSb NWs with a larger GaAs core is shown in Figures S16 and S17. It is interesting to find that for bare GaAs NWs (Figures S18–S21), regardless of the size of the GaAs NWs, their crystal structure shows WZ/ZB mixed-phases. It is needed to mention that Sb has been incorporated into III–V semiconductor NWs as surfactant to modify the crystal structure of the material.<sup>44–46</sup> In contrast, we grow GaAs core first and then GaAsSb shell, where Sb component is in the shell layer but not the core. Therefore, the surfactant effect of Sb to modify the GaAs core can be ruled out. For GaAs/GaAsSb core-shell NWs discussed herein, both pure ZB phase and WZ/ZB mixed-phases have been observed, which is found to be related to the size of GaAs core. This size-dependent phenomenon will be discussed later.

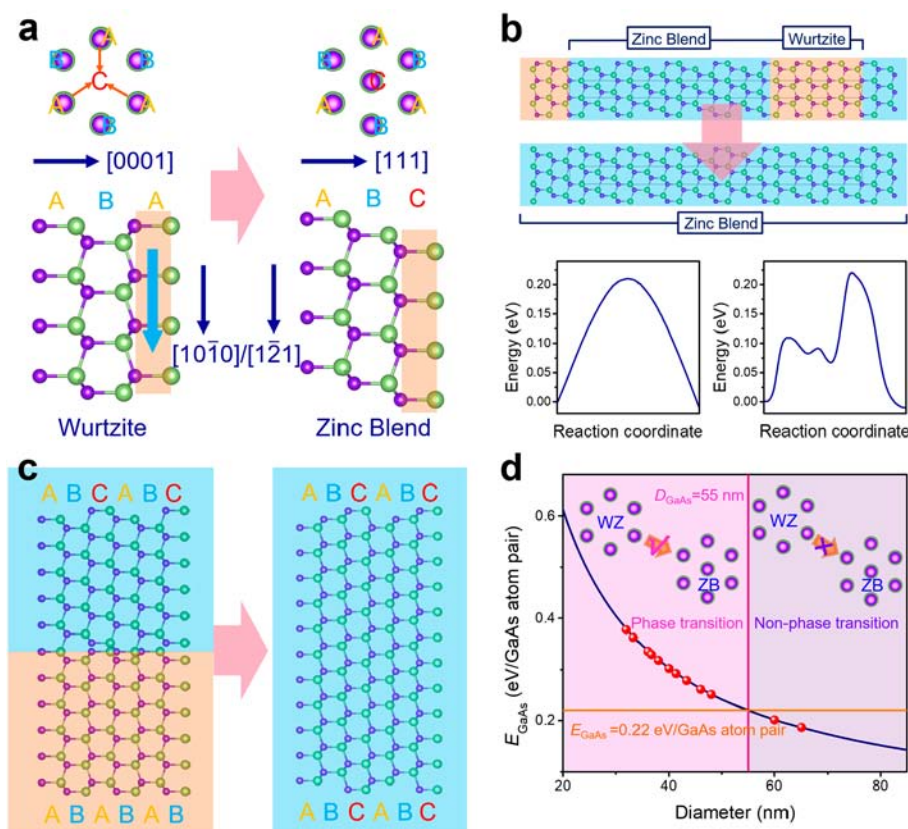


**Figure 4.** Mechanism of transformations from WZ to ZB. (a) Schematic diagram of the transformations from WZ to ZB. (b) The schematic graph of the GaAs phase transition (top panel). Energy transition barrier obtained from the dislocation theory (left panel) and the NEB calculation (right panel). (c) Atomic model of WZ and ZB in radial direction of NW. (d) The relationship between the maximum energy of phase transition and the diameter of the GaAs core.

The HRTEM image of the interface between the GaAs/GaAsSb core–shell and GaAsSb is shown in Figure 3g, where a twin plane is indicated by white arrow. The lattice sequences of ZB structure is ABCABC and misplacement of a bilayer to yield a sequence of ABCABC $\bar{C}$ BACBA results in a symmetry structure with a mirror plane  $\bar{A}$ , which is known as a twin plane. The twinning angle is measured to be about  $141^\circ$  ( $70.5^\circ + 70.5^\circ$ ), which is in accordance with the relative rotational angle of (111) twin crystals in face centered cubic (fcc) structures. Moreover, the FFT pattern reveals that the crystalline phase is a pure ZB structure. Figure 3h shows a HRTEM of the GaAsSb NW, while the inset displays the corresponding FFT pattern. Again, it can be clearly seen that the GaAsSb NW is a pure ZB phase. Consequently, the entire GaAs/GaAsSb NW is the perfect single-phase.

Figure 4a shows the schematic diagram of the transformations from WZ to ZB crystal structure due to partial dislocations. WZ and ZB structures can be described as stacks of Ga–As monolayers (MLs) along the  $[0001]_{\text{WZ}}/[111]_{\text{ZB}}$ . The two stacking modes are usually denoted as ABABAB... (WZ) and ABCABC... (ZB), where the letters represent distinct positions of the ML (Figure 4a). Due to the influence of external force, the Ga–As ML slips from point A to point C, which leads to the transformation of the ABA structure to ABC. The slip direction is  $[10\bar{1}0]_{\text{WZ}}/[1\bar{2}1]_{\text{ZB}}$ . Similarly, the stacking faults and twins will be eliminated due to the atomic rearrangement. According to the established phases transition model (top panel of Figure 4b), the maximum energy required to transform the single GaAs atom pair from the WZ to ZB

structure is calculated by the dislocation theory<sup>29,33</sup> (left panel of Figure 4b) and the nudged elastic band (NEB)<sup>47,48</sup> (right panel of Figure 4b). Details of the calculations are provided in the Supporting Information. The maximum transition barrier obtained from these calculations is the same as 0.22 eV/GaAs atom pair.

At the same time, the Shockley partial dislocations theory<sup>49,50</sup> has been employed to analyze the transition mechanism. The crystal structures at the interface before and after transformation are shown in Figure 4c. The difference of interplanar spacing between GaAs  $(0001)_{\text{WZ}}$  and GaAsSb  $(111)_{\text{ZB}}$  is negligible, and the stress is perpendicular to the slip plane, which has no contribution to the transformation. However, the different atomic arrangements between the  $(0001)_{\text{WZ}}/(111)_{\text{ZB}}$  plane should be taken into consideration. It will introduce stress perpendicular to the interface of core ( $(10\bar{1}0)_{\text{WZ}}$ ) and shell ( $(1\bar{2}1)_{\text{ZB}}$ ), which leads to the slip of Ga–As MLs and promotes the rearrangement atoms. The six GaAs MLs ABABAB (WZ) and ABCABC (ZB) sequences are the minimum repeated units at the core–shell interface. In one period, only two GaAs MLs are matched, and the other four MLs are lattice mismatched, as shown in Figure 4c (left panel). The shear tension and the strain energy at the interface between the shell and core during the transformation process are calculated. The detailed calculation process can be found in Figures S22 and S23. As a result, the relationship of the maximum energy per GaAs atom pair and the GaAs NW diameter is constructed, and the curve is plotted in Figure 4d. We have measured a series of GaAs/GaAsSb core–shell NWs

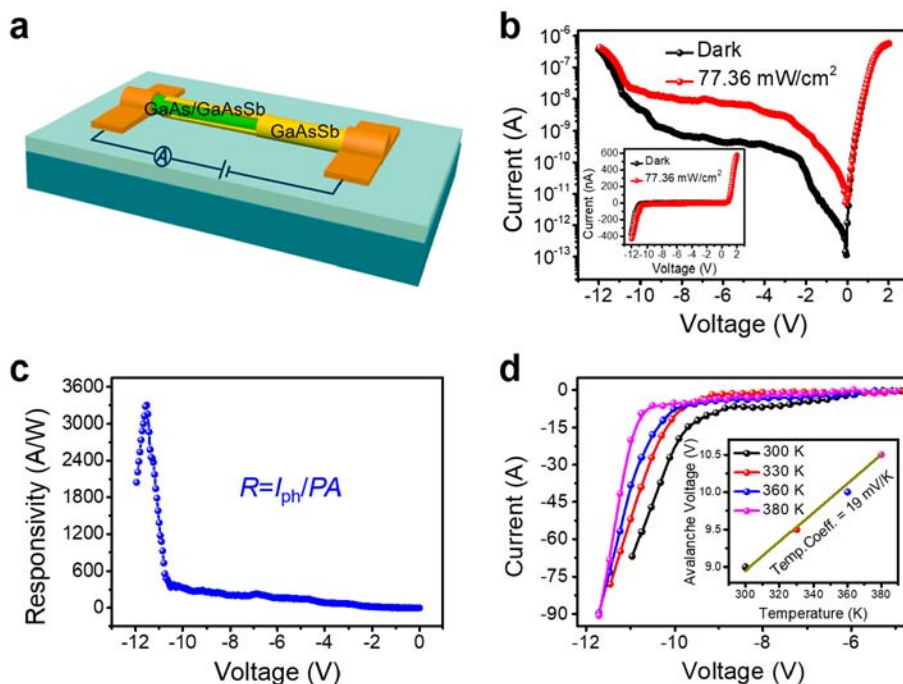


**Figure 5.** Photodetection performance of GaAs/GaAsSb NW APD (532 nm laser). (a) Schematic diagram of GaAs/GaAsSb NW APD device. (b) The  $I$ – $V$  characteristics of the APD device under dark conditions and 532 nm light illumination with a density of 77.36 mW/cm<sup>2</sup>. Inset is the  $I$ – $V$  characteristic curves in normal coordinates. (c) Responsivity of the APD device. (d)  $I$ – $V$  characteristics at 300–380 K in the reverse voltage under dark conditions, and the inset shows the dependence of the avalanche breakdown voltage with temperature.

with different GaAs core diameters. It shows that when the GaAs core diameter is smaller than 55 nm, the GaAs/GaAsSb core–shell crystal structure is of the pure ZB phase. In comparison, when the GaAs core diameter is bigger than 55 nm, the maximum energy received from the interfacial stress is not sufficient for phase transition and NW is either WZ/ZB mixed-phases or a ZB structure with defects. The experimental results are consistent with the theoretical calculations. Therefore, the critical diameter of GaAs core for successful phase transition can be determined to be 55 nm.

The unique property of single crystal benefits nano-optoelectronics devices. The schematic diagram of the GaAs/GaAsSb NW photodiode is shown in Figure 5a. Figure 5b shows the current–voltage ( $I$ – $V$ ) characteristic curves of the pure ZB phase GaAs/GaAsSb heterojunction photodiode. The inset of Figure 5b shows the dark and photocurrent of the GaAs/GaAsSb heterojunction photodiode in linear scale. The  $I$ – $V$  curves present the characteristic of forward conducting and reverse cutoff, as shown in Figure 5b. When the reverse voltage is higher than 11 V, the current increases dramatically, which implies the breakdown of the photodiode. To show the response of the current to the incident optical power, the responsivity ( $R$ ) can be calculated by using the equation

$$R = (I_{\text{light}} - I_{\text{dark}}) / (P \times A) \quad (1)$$

where  $I_{\text{light}}$  is the current under illumination,  $I_{\text{dark}}$  is the current before illumination,  $P$  is the power intensity, and  $A$  is the effective illuminated area.<sup>22,51</sup> When the reverse bias is near 11.5 V, the responsivity reaches a maximum of  $3.3 \times 10^3$  A/W (Figure 5c).

Figure 5d shows the reverse  $I$ – $V$  curves under a temperature from 300 to 380 K, from where the increases of the breakdown voltage (from  $-9.0$  to  $-10.6$  V) can be clearly observed. A

positive temperature coefficient of 19 mV/K is obtained for this device, which supports the avalanche breakdown phenomenon. These results suggest that our device is an APD, and the avalanche multiplication dominates the internal gain. The multiplication factor ( $M_a$ ) of the heterojunction structure can be determined using

$$M_a = (I_{\text{ph}} - I_{\text{d}}) / (I_{\text{ph0}} - I_{\text{d0}}) \quad (2)$$

where  $I_{\text{ph}}$  and  $I_{\text{d}}$  are the multiplied photocurrent and dark current, and  $I_{\text{ph0}}$  and  $I_{\text{d0}}$  are the unmultiplied photocurrent and dark current, respectively.<sup>51,52</sup> The  $M_a$  of the APD device reaches a maximum value of  $8.62 \times 10^3$  under the reverse bias of 11.5 V, which is larger than the value of GaAs nanopillar APDs (216).<sup>53</sup> The excellent performances are mainly ascribed to the single crystal structure of GaAs/GaAsSb NWs. In single crystal NWs, there are no polytype boundaries, twin-planes, stacking faults, and so on, which reduce the scattering of carriers and decrease the uncertainty of collision ionization.

## CONCLUSIONS

In conclusion, we propose a novel approach to achieve pure-phase single crystal NWs by stress, which is verified by  $\mu$ -Raman spectroscopy and atomic-level TEM. In III–V core–shell NWs, the crystal structure is related to the size of the core NW. The Shockley partial dislocations theory is used to calculate the shear tension and strain energy at the core–shell interface, which reveals the underlying physical mechanism in accompany with first-principles energy barrier calculations. The critical diameter of the GaAs core for the phase transition is evaluated to be 55 nm. An APD has been fabricated based on the pure ZB phase GaAs/GaAsSb NW, which shows a high performance in terms of high responsivity ( $3.3 \times 10^3$  A/W) and a superior multiplication factor ( $8.62 \times 10^3$ ) under  $-11.5$

V bias. Our work opens the door for the crystal phase control of nanomaterials and performance improvement of optoelectronics devices in the future.

## ■ ASSOCIATED CONTENT

### SI Supporting Information

The Supporting Information is available free of charge at <https://pubs.acs.org/doi/10.1021/acsp Photonics.1c01196>.

Experimental methods (substrate treatment, NWs growth, material characterizations, detector fabrication, device characterization, and first-principles calculations); the morphology of GaAs NWs, the EDXs, and mapping of GaAs/GaAsSb NW; the Raman and  $\mu$ -Raman spectra of GaAs and GaAs/GaAsSb NWs; the TEM images of GaAs and GaAs/GaAsSb NWs; the strain of GaAs/GaAsSb core-shell structure (PDF)

## ■ AUTHOR INFORMATION

### Corresponding Authors

**Zhipeng Wei** – State Key Laboratory of High Powder Semiconductor Lasers, Changchun University of Science and Technology, Changchun 130022, China; [orcid.org/0000-0002-0492-9365](https://orcid.org/0000-0002-0492-9365); Email: [zpweicust@126.com](mailto:zpweicust@126.com)

**Rui Chen** – Department of Electrical and Electronic Engineering, Southern University of Science and Technology, Guangdong 518055, China; [orcid.org/0000-0002-0445-7847](https://orcid.org/0000-0002-0445-7847); Email: [chenr@sustech.edu.cn](mailto:chenr@sustech.edu.cn)

### Authors

**Yubin Kang** – State Key Laboratory of High Powder Semiconductor Lasers, Changchun University of Science and Technology, Changchun 130022, China

**Guangren Na** – State Key Laboratory of Integrated Optoelectronics, Key Laboratory of Automobile Materials of MOE, School of Materials Science and Engineering, Jilin University, Changchun 130012, China

**Dengkui Wang** – State Key Laboratory of High Powder Semiconductor Lasers, Changchun University of Science and Technology, Changchun 130022, China; [orcid.org/0000-0002-4787-7710](https://orcid.org/0000-0002-4787-7710)

**Jilong Tang** – State Key Laboratory of High Powder Semiconductor Lasers, Changchun University of Science and Technology, Changchun 130022, China

**Lijun Zhang** – State Key Laboratory of Integrated Optoelectronics, Key Laboratory of Automobile Materials of MOE, School of Materials Science and Engineering, Jilin University, Changchun 130012, China; [orcid.org/0000-0002-6438-5486](https://orcid.org/0000-0002-6438-5486)

**Yabing Shan** – State Key Laboratory of ASIC and System, School of Information Science and Technology, Fudan University, Shanghai 200433, China

**Chunxiao Cong** – State Key Laboratory of ASIC and System, School of Information Science and Technology, Fudan University, Shanghai 200433, China; [orcid.org/0000-0001-9786-825X](https://orcid.org/0000-0001-9786-825X)

Complete contact information is available at: <https://pubs.acs.org/doi/10.1021/acsp Photonics.1c01196>

### Author Contributions

<sup>#</sup>Y.K. and G.N. contributed equally to this work. Z.W. and R.C. supervised the project. Y.K. performed most of the experiments. J.T. and Y.K. contributed to material preparations and

characterizations. L.Z. and G.N. contributed to first-principles simulation. Y.S. and C.C. contributed to the  $\mu$ -Raman spectroscopy measurements. D.W. fabricated the NW devices. Y.K., D.W., Z.W., and R.C. analyzed the data and cowrote the paper. All authors examined and commented on the manuscript.

### Notes

The authors declare no competing financial interest.

## ■ ACKNOWLEDGMENTS

This work was supported by the National Natural Science Foundation of China (61674021, 11674038, 61704011, 61904017), the Developing Project of Science and Technology of Jilin Province (20200301052RQ), the Project of Education Department of Jilin Province (JJKH20200763KJ) and The Youth Foundation of Changchun University of Science and Technology (XQNJJ-2018-18).

## ■ REFERENCES

- (1) del Alamo, J. A. Nanometre-Scale Electronics with III-V Compound Semiconductors. *Nature* **2011**, *479*, 317–323.
- (2) Yan, R. X.; Gargas, D.; Yang, P. D. Nanowire Photonics. *Nat. Photonics* **2009**, *3*, 569–576.
- (3) Patolsky, F.; Zheng, G.; Lieber, C. M. Nanowire Sensors for Medicine and the Life Sciences. *Nanomedicine* **2006**, *1*, 51–65.
- (4) Dai, X.; Zhang, S.; Wang, Z.; Adamo, G.; Liu, H.; Huang, Y.; Couteau, C.; Soci, C. GaAs/AlGaAs Nanowire Photodetector. *Nano Lett.* **2014**, *14*, 2688–2693.
- (5) Zhu, X. T.; Lin, F. Y.; Zhang, Z. H.; Chen, X.; Huang, H.; Wang, D. K.; Tang, J. L.; Fang, X.; Fang, D.; Ho, J. C.; Liao, L.; Wei, Z. P. Enhancing Performance of a GaAs/AlGaAs/GaAs Nanowire Photodetector Based on the Two-Dimensional Electron–Hole Tube Structure. *Nano Lett.* **2020**, *20*, 2654–2659.
- (6) Tomioka, K.; Yoshimura, M.; Fukui, T. A III-V Nanowire Channel on Silicon for High-Performance Vertical Transistors. *Nature* **2012**, *488*, 189–192.
- (7) Dimakis, E.; Jahn, U.; Ramsteiner, M.; Tahraoui, A.; Grandal, J.; Kong, X.; Marquardt, O.; Trampert, A.; Riechert, H.; Geelhaar, L. Coaxial multishell (In, Ga) As/GaAs nanowires for near-infrared emission on Si substrates. *Nano Lett.* **2014**, *14*, 2604–2609.
- (8) Krogstrup, P.; Jorgensen, H. I.; Heiss, M.; Demichel, O.; Holm, J. V.; Aagesen, M.; Nygård, J.; Fontcuberta i Morral, A. Single-Nanowire Solar Cells Beyond the Shockley-Queisser Limit. *Nat. Photonics* **2013**, *7*, 306–310.
- (9) Saxena, D.; Mokkaapati, S.; Parkinson, P.; Jiang, N.; Gao, Q.; Tan, H. H.; Jagadish, C. Optically pumped room-temperature GaAs nanowire lasers. *Nat. Photonics* **2013**, *7*, 963–968.
- (10) Thelander, C.; Nilsson, H. A.; Jensen, L. E.; Samuelson, L. Nanowire single-electron memory. *Nano Lett.* **2005**, *5*, 635–638.
- (11) Hahn, J.; Lieber, C. M. Direct ultrasensitive electrical detection of DNA and DNA sequence variations using nanowire nanosensors. *Nano Lett.* **2004**, *4*, 51–54.
- (12) Dayeh, S. A.; Susac, D.; Kavanagh, K. L.; Yu, E. T.; Wang, D. Structural and Room-Temperature Transport Properties of Zinc Blende and Wurtzite InAs Nanowires. *Adv. Funct. Mater.* **2009**, *19*, 2102–2108.
- (13) Fu, M.; Tang, Z.; Li, X.; Ning, Z.; Pan, D.; Zhao, J.; Wei, X.; Chen, Q. Crystal Phase and Orientation-Dependent Electrical Transport Properties of InAs Nanowires. *Nano Lett.* **2016**, *16*, 2478–2484.
- (14) Zardo, I.; Conesa-Boj, S.; Peiro, F.; Morante, J. R.; Arbiol, J.; Uccelli, E.; Abstreiter, G.; Fontcuberta i Morral, A. Raman Spectroscopy of Wurtzite and Zinc-Blende GaAs Nanowires: Polarization Dependence, Selection Rules, and Strain Effects. *Phys. Rev. B: Condens. Matter Mater. Phys.* **2009**, *80*, 245324.
- (15) Spirkoska, D.; Arbiol, J.; Gustafsson, A.; Conesa-Boj, S.; Glas, F.; Zardo, I.; Heigoldt, M.; Gass, M. H.; Bleloch, A. L.; Estrade, S.; Kaniber, M.; Rossler, J.; Peiro, F.; Morante, J. R.; Abstreiter, G.;

Samuelson, L.; Fontcuberta i Morral, A. Structural and optical properties of high quality zinc-blende/wurtziteGaAs heteronanowires. *Phys. Rev. B: Condens. Matter Mater. Phys.* **2009**, *80*, 245325.

(16) Jahn, U.; Lähnemann, J.; Pfüller, C.; Brandt, O.; Breuer, S.; Jenichen, B.; Ramsteiner, M.; Geelhaar, L.; Riechert, H. Luminescence of GaAs nanowires consisting of wurtzite and zinc-blende segments. *Phys. Rev. B: Condens. Matter Mater. Phys.* **2012**, *85*, 045323.

(17) Thelander, C.; Caroff, P.; Plissard, S.; Dey, A. W.; Dick, K. A. Effects of crystal phase mixing on the electrical properties of InAs nanowires. *Nano Lett.* **2011**, *11*, 2424–2429.

(18) Parkinson, P.; Joyce, H. J.; Gao, Q.; Tan, H. H.; Zhang, X.; Zou, J.; Jagadish, C.; Herz, L. M.; Johnston, M. B. Carrier Lifetime and Mobility Enhancement in Nearly Defect-Free Core Shell Nanowires Measured Using Time-Resolved Terahertz Spectroscopy. *Nano Lett.* **2009**, *9*, 3349–3353.

(19) Woo, R. L.; Xiao, R.; Kobayashi, Y.; Gao, L.; Goel, N.; Hudait, M. K.; Mallouk, T. E.; Hicks, R. F. Effect of twinning on the photoluminescence and photoelectrochemical properties of indium phosphide nanowires grown on silicon (111). *Nano Lett.* **2008**, *8*, 4664–4669.

(20) Knutsson, J. V.; Lehmann, S.; Hjort, M.; Lundgren, E.; Dick, K. A.; Timm, R.; Mikkelsen, A. Electronic Structure Changes Due to Crystal Phase Switching at the Atomic Scale Limit. *ACS Nano* **2017**, *11*, 10519–10528.

(21) Hjort, M.; Lehmann, S.; Knutsson, J.; Timm, R.; Jacobsson, D.; Lundgren, E.; Dick, K. A.; Mikkelsen, A. Direct Imaging of Atomic Scale Structure and Electronic Properties of GaAs Wurtzite and Zinc Blende Nanowire Surfaces. *Nano Lett.* **2013**, *13*, 4492–4498.

(22) Ali, H.; Zhang, Y.; Tang, J.; Peng, K.; Sun, S.; Sun, Y.; Song, F.; Falak, A.; Wu, S.; Qian, C.; Wang, M.; Zuo, Z.; Jin, K.-J.; Sanchez, A. M.; Liu, H.; Xu, X. High-Responsivity Photodetection by a Self-Catalyzed Phase-Pure p-GaAs Nanowire. *Small* **2018**, *14*, 1704429.

(23) Caroff, P.; Dick, K. A.; Johansson, J.; Messing, M. E.; Deppert, K.; Samuelson, L. Controlled Polytypic and Twin-Plane Superlattices in III-V Nanowires. *Nat. Nanotechnol.* **2009**, *4*, 50–55.

(24) Gil, E.; Dubrovskii, V. G.; Avit, G.; Andre, Y.; Leroux, C.; Lekhal, K.; Grecenkov, J.; Travers, A.; Castellucci, D.; Monier, G.; Ramdani, R. M.; Robert-Goumet, C.; Bideux, L.; Harmand, J. C.; Glas, F. Record Pure Zincblende Phase in GaAs Nanowires Down to 5 nm in Radius. *Nano Lett.* **2014**, *14*, 3938–3944.

(25) Pan, D.; Fu, M.; Yu, X.; Wang, X.; Zhu, L.; Nie, S.; Wang, S.; Chen, Q.; Xiong, P.; von Molnar, S.; Zhao, J. Controlled Synthesis of Phase-Pure InAs Nanowires on Si (111) by Diminishing the Diameter to 10 nm. *Nano Lett.* **2014**, *14*, 1214–1220.

(26) Ketterer, B.; Heiss, M.; Uccelli, E.; Arbiol, J.; Fontcuberta i Morral, A. Untangling the Electronic Band Structure of Wurtzite GaAs Nanowires by Resonant Raman Spectroscopy. *ACS Nano* **2011**, *5*, 7585–7592.

(27) Lehmann, S.; Wallentin, J.; Jacobsson, D.; Deppert, K.; Dick, K. A. A General Approach for Sharp Crystal Phase Switching in InAs, GaAs, InP, and GaP Nanowires Using Only Group V Flow. *Nano Lett.* **2013**, *13*, 4099–4105.

(28) Panciera, F.; Baraissov, Z.; Patriarche, G.; Dubrovskii, V. G.; Glas, F.; Travers, L.; Mirsaidov, U.; Harmand, J. C. Phase Selection in Self-catalyzed GaAs Nanowires. *Nano Lett.* **2020**, *20*, 1669–1675.

(29) Zheng, H.; Wang, J.; Huang, J. Y.; Wang, J.; Zhang, Z.; Mao, S. X. Dynamic process of phase transition from wurtzite to zinc blende structure in InAs nanowires. *Nano Lett.* **2013**, *13*, 6023–6027.

(30) Jacobsson, D.; Panciera, F.; Tersoff, J.; Reuter, M. C.; Lehmann, S.; Hofmann, S.; Dick, K. A.; Ross, F. M. Interface Dynamics and Crystal Phase Switching in GaAs Nanowires. *Nature* **2016**, *531*, 317–322.

(31) Loitsch, B.; Rudolph, D.; Morkötter, S.; Döblinger, M.; Grimaldi, G.; Hanschke, L.; Matich, S.; Parzinger, E.; Wurstbauer, U.; Abstreiter, G.; Finley, J. J.; Koblmüller, G. Tunable Quantum Confinement in Ultrathin, Optically Active Semiconductor Nanowires Via Reverse-Reaction Growth. *Adv. Mater.* **2015**, *27*, 2195–2202.

(32) Ilkiv, I.; Kirilenko, D.; Kotlyar, K.; Bouravlevu, A. Thermal decomposition of GaAs nanowires. *Nanotechnology* **2020**, *31*, 055701.

(33) Patriarche, G.; Glas, F.; Tchernycheva, M.; Sartet, C.; Largeau, L.; Harmand, J.-C.; Cirlin, G. E. Wurtzite to zinc blende phase transition in GaAs nanowires induced by epitaxial burying. *Nano Lett.* **2008**, *8*, 1638–1643.

(34) Algra, R. E.; Verheijen, M. A.; Borgstrom, M. T.; Feiner, L.-F.; Immink, G.; van Enckevort, W. J. P.; Vlieg, E.; Bakkers, E. P. A. M. Twinning Superlattices in Indium Phosphide Nanowires. *Nature* **2008**, *456*, 369–372.

(35) Lu, Z.; Zhang, Z.; Chen, P.; Shi, S.; Yao, L.; Zhou, C.; Zhou, X.; Zou, J.; Lu, W. Bismuth-induced phase control of GaAs nanowires grown by molecular beam epitaxy. *Appl. Phys. Lett.* **2014**, *105*, 162102.

(36) Ren, D.; Dheeraj, D. L.; Jin, C.; Nilsen, J. S.; Huh, J.; Reinertsen, J. F.; Munshi, A. M.; Gustafsson, A.; van Helvoort, A. T. J. V.; Fimland, B. O.; Weman, H. New insights into the origins of Sb-induced effects on self-catalyzed GaAsSb nanowire arrays. *Nano Lett.* **2016**, *16*, 1201–1209.

(37) Potts, H.; Friedl, M.; Amaduzzi, F.; Tang, K. C.; Tütüncüoğlu, G.; Matteini, F.; Lladó, E. A.; McIntyre, P. C.; Fontcuberta i Morral, A. From twinning to pure zincblende catalyst-free InAs (Sb) nanowires. *Nano Lett.* **2016**, *16*, 637–643.

(38) Mahan, G. D.; Gupta, R.; Xiong, Q.; Adu, C. K.; Eklund, P. C. Optical phonons in polar semiconductor nanowires. *Phys. Rev. B: Condens. Matter Mater. Phys.* **2003**, *68*, 073402.

(39) Zardo, L.; Yazji, S.; Marini, C.; Uccelli, E.; Fontcuberta i Morral, A.; Abstreiter, G.; Postorino, P. Pressure Tuning of the Optical Properties of GaAs Nanowires. *ACS Nano* **2012**, *6*, 3284–3291.

(40) Signorello, G.; Karg, S.; Björk, M. T.; Gotsmann, B.; Riel, H. Tuning the Light Emission from GaAs Nanowires over 290 meV with Uniaxial Strain. *Nano Lett.* **2013**, *13*, 917–924.

(41) Signorello, G.; Loertscher, E.; Khomyakov, P. A.; Karg, S.; Dheeraj, D. L.; Gotsmann, B.; Weman, H.; Riel, H. Inducing a Direct-to-Pseudodirect Bandgap Transition in Wurtzite GaAs Nanowires with Uniaxial Stress. *Nat. Commun.* **2014**, *5*, 3655.

(42) Alarcón-Lladó, E.; Conesa-Boj, S.; Wallart, X.; Caroff, P.; Fontcuberta i Morral, A. Raman spectroscopy of self-catalyzed GaAs<sub>1-x</sub>Sb<sub>x</sub> nanowires grown on silicon. *Nanotechnology* **2013**, *24*, 405707.

(43) Li, L.; Pan, D.; Xue, Y.; Wang, X.; Lin, M.; Su, D.; Zhang, Q.; Yu, X.; So, H.; Wei, D.; Sun, B.; Tan, P.; Pan, A.; Zhao, J. Near Full-Composition-Range High-Quality GaAs<sub>1-x</sub>Sb<sub>x</sub> Nanowires Grown by Molecular-Beam Epitaxy. *Nano Lett.* **2017**, *17*, 622–630.

(44) Dheeraj, D. L.; Patriarche, G.; Zhou, H. L.; Hoang, T. B.; Moses, A. F.; Gronsborg, S.; van Helvoort, A. T. J.; Fimland, B. O.; Weman, H. Growth and Characterization of Wurtzite GaAs Nanowires with Defect-Free Zinc Blende GaAsSb Inserts. *Nano Lett.* **2008**, *8*, 4459–4463.

(45) Plissard, S. R.; Dick, K. A.; Wallart, X.; Caroff, P. Gold-Free GaAs/GaAsSb Heterostructure Nanowires Grown on Silicon. *Appl. Phys. Lett.* **2010**, *96*, 121901.

(46) Zhuang, Q. D.; Anyebe, E. A.; Chen, R.; Liu, H.; Sanchez, A. M.; Rajpalke, M. K.; Veal, T. D.; Wang, Z. M.; Huang, Y. Z.; Sun, H. D. Sb-Induced Phase Control of InAsSb Nanowires Grown by Molecular Beam Epitaxy. *Nano Lett.* **2015**, *15*, 1109–1116.

(47) Henkelman, G.; Uberuaga, B. P.; Jónsson, H. A climbing image nudged elastic band method for finding saddle points and minimum energy paths. *J. Chem. Phys.* **2000**, *113*, 9901–9904.

(48) Henkelman, G.; Jónsson, H. Improved tangent estimate in the nudged elastic band method for finding minimum energy paths and saddle points. *J. Chem. Phys.* **2000**, *113*, 9978–9985.

(49) Poh, K. W. Stress-strain-temperature relationship for structural steel. *J. Mater. Civ. Eng.* **2001**, *13*, 371–379.

(50) Carden, W. D.; Geng, L. M.; Matlock, D. K.; Wagoner, R. H. Measurement of springback. *Int. J. Mech. Sci.* **2002**, *44*, 79–101.

(51) Zhao, B.; Wang, F.; Chen, H.; Wang, Y.; Jiang, M.; Fang, X.; Zhao, D. Solar-Blind Avalanche Photodetector Based On Single ZnO-Ga<sub>2</sub>O<sub>3</sub> Core-Shell Microwire. *Nano Lett.* **2015**, *15*, 3988–3993.

(52) Hayden, O.; Agarwal, R.; Lieber, C. M. Nanoscale avalanche photodiodes for highly sensitive and spatially resolved photon detection. *Nat. Mater.* **2006**, *5*, 352–356.

(53) Senanayake, P.; Hung, C.-H.; Farrell, A.; Ramirez, D. A.; Shapiro, J.; Li, C.-K.; Wu, Y. R.; Hayat, M. M.; Huffaker, D. L. Thin 3D multiplication regions in plasmonically enhanced nanopillar avalanche detectors. *Nano Lett.* **2012**, *12*, 6448–6452.